PAPER

Check for updates

Temperature response of defect photoluminescence in locally functionalized single-walled carbon nanotubes†

Ryo Hamano, [a] Yoshiaki Niidome,[a] Naoki Tanaka,[ab] Tomohiro Shiraki [ab] and Tsuyohiko Fujigaya [abc]

In vivo temperature monitoring has garnered significant attention for studying biological processes such as cellular differentiation and enzymatic activity. However, current nanoscale thermometers utilizing photoluminescence (PL) in the visible to first near-infrared (NIR-I) region based on organic dyes, quantum dots, and lanthanide-doped nanoparticles face challenges in terms of tissue penetration and sensitivity. In this study, we investigated the temperature dependence of E_{11}^* PL (1140 nm) and E_{11}^{*-} PL (1260 nm) of locally functionalized single-walled carbon nanotubes (lf-SWCNTs) that emit in the second near-infrared region (NIR-II). The effects of interfacial dielectric environments (hydrophobic surfactant dispersion *vs.* hydrophilic gel coating), defect density, and nanotube length on the temperature responsiveness were systematically examined. The results demonstrated that E_{11}^* PL was more sensitive to temperature changes than E_{11}^{*-} PL and lf sites having a lower dielectric environment further enhanced temperature responsiveness. Additionally, longer lf-SWCNTs exhibited greater temperature responsiveness than the shorter ones. These findings provide valuable insights into optimizing gel-coated lf-SWCNTs to achieve higher temperature responsiveness and develop biocompatible temperature sensors capable of monitoring deep tissues within complex biological environments.

Introduction

Monitoring local temperature variations *in vivo* is a powerful tool for understanding biological processes such as cell differentiation, enzymatic reactions, and immune responses.[1–3] Consequently, there has been extensive research into temperature monitoring and imaging in cells and tissues through the photoluminescence (PL) responses of dyes and transition-metal ions. Temperature monitoring using PL by observing intensity changes, wavelength shifts, and lifetime adjustments is an attractive, non-invasive approach with high spatial resolution. Organic dyes,[4,5] quantum dots,[6,7] up-conversion nanoparticles,[8,9] and nanodiamonds[10,11] have been used as temperature indicators in biological systems. However, most of these nanomaterials operate in the visible (400–700 nm) to first near-infrared (NIR-I) range (700–1000 nm), limiting their monitoring depth to less than 2–5 mm owing to light scattering and absorption in biological tissues. Therefore, in recent years, lanthanide ion-doped nanoparticles have been developed as luminescent thermometers in the second near-infrared range (NIR-II: 1000–1700 nm),[12–15] which have high biological permeability (5–20 mm). However, because lanthanide ion-based nanoparticles use luminescence caused by the forbidden f–f transition, they inherently have low fluorescence quantum yields and are also toxic to the body.[16,17] Therefore, there is a great demand for the development of brighter and more biocompatible fluorescent temperature sensors in the NIR-II region.

Single-walled carbon nanotubes (SWCNTs)[18] exhibit unique photo-absorption and PL characteristics in the NIR-II region,[19] offering deep tissue permeation and making them promising for *in vivo* imaging applications.[20,21] The PL of SWCNTs, which originates from excitons confined in one dimension, is temperature-dependent[22,23] and responsive to changes in the surrounding dielectric environment.[24] This responsiveness positions SWCNTs as promising materials for *in vivo* monitoring, not only for temperature changes but also for interactions with surrounding molecules.[25–28] Furthermore, SWCNTs can be covalently or non-covalently modified on their surface, allowing for enhanced responsiveness or selectivity in biological interactions. However, a significant limitation of SWCNTs in biological applications is their relatively low PL quantum yield compared to that of conventional luminescent materials in the

aDepartment of Applied Chemistry, Graduate School of Engineering, Kyushu University, 744 Motooka, Fukuoka 819-0395, Japan. E-mail: fujigaya.tsuyohiko.948@m.kyushu-u.ac.jp

bInternational Institute for Carbon Neutral Energy Research (WPI I²CNER), Kyushu University, 744 Motooka, Fukuoka 819-0395, Japan

cCenter for Molecular Systems (CMS), Kyushu University, 744 Motooka, Fukuoka 819-0395, Japan

visible range. This limitation primarily arises from reabsorption due to small Stokes shifts and nonradiative decay caused by exciton diffusion to structural defects or quenching sites at the tube ends.[29–34]

Low-density covalent modifications of SWCNTs prepared with ozone,[35] halides,[36] and aryl diazonium salts[37] have been recently reported to create new emissive sites known as quantum defects or local functionalization (lf) sites.[38–40] These lf sites act as potential barriers and efficiently localize excitons at lower energy levels, resulting in brighter and red-shifted (100–250 meV) PL (E_{11}^* PL) compared to the native E_{11} PL. This significant red shift enables NIR-II emission through localized excitation by NIR-II excitation, which is a notable advantage for biological applications.[41–50]

In 2010, Weisman et al. first reported the generation of E_{11}^* PL in ozone-doped SWCNTs and noted its temperature dependency.[35] They calculated the thermal de-trapping energy from the slope of the van't Hoff plots (natural logarithm of E_{11}/E_{11}^* intensity ratio vs. inverse temperature) and found that these values were less than half of the trapping energy, comparable in magnitude to thermal energy (kT). In 2016, Wang et al. highlighted the utility of lf-PL for temperature sensing in biological applications using aryl-modified lf-SWCNTs.[51] They cited two main reasons: (1) E_{11}^* PL was more pronounced in response to temperature than E_{11} PL, and (2) the PL intensity ratio of E_{11}/E_{11}^* provided a more reliable local temperature measurement, as both the probe (E_{11}^* PL) and internal reference (E_{11} PL) existed in the same chemical environment, whereas the E_{11} PL of pristine SWCNTs was responsive not only to temperature but also to other environmental changes. Given their strong potential for sensitive temperature monitoring, further analysis is required to understand the factors influencing their responsiveness.

In this study, we investigated the temperature dependence of lf-PL, focusing not only on E_{11}^* PL, but also on E_{11}^{*-} PL, to assess the effect of the trapping energy depth on the temperature responsiveness. In addition, we examined the effects of the dielectric environment (hydrophobic vs. hydrophilic), defect density, and tube length. For the lf sites, two distinct aryl modifications (para-nitro benzenediazonium tetrafluoroborate[37] and ortho-phenyl benzenediazonium tetrafluoroborate[52]) that selectively emit E_{11}^* and E_{11}^{*-} PL, respectively, were employed. To provide a hydrophilic environment for the lf sites, we used gel-coating of lf-SWCNTs prepared by radical polymerization in the presence of surfactants, called "CNT Micelle Polymerization".[53–62] Specifically, PEG methacrylate was chosen as the monomer to form a gel layer around lf-SWCNTs, ensuring stable dispersion in aqueous systems.[53,56] Surfactant-dispersed lf-SWCNTs served as the hydrophobic counterpart. Previously, we reported that PEG-containing gel-coated SWCNTs are suitable for NIR-II imaging in vivo because of their excellent dispersion stability, biocompatibility, and bright NIR-II PL, all of which are desirable for in vivo applications.[62] Therefore, gel-coated lf-SWCNTs can be readily applied as in vivo temperature sensors if the temperature-dependent changes are sufficiently large. In addition to the benefits of gel coating, we demonstrated that gel-coated SWCNTs can be sorted by

length using chromatography,[61] allowing us to study the effects of tube length on the temperature-dependent lf-PL.

Experimental

Materials

(6, 5)-rich SWCNTs (CoMoCAT, Lot#MKVZ1159V, Sigma-Aldrich Co. LLC, Saint Louis, USA), sodium dodecyl sulfate (SDS), polyethylene glycol methacrylate (PEGMA; $M_n \sim 500$), maleimide, furan, and ×100 Tris-EDTA (TE) buffer solution (pH 8.0) were purchased from Sigma-Aldrich (Tokyo, Japan). Deuterated water (D_2O) was purchased from Cambridge Isotope Laboratories Inc. (Tewksbury, MA, USA). N,N′-Methylenebisacrylamide (BIS), tetramethylethylenediamine (TMEDA), and ammonium persulfate (APS) were purchased from Wako Pure Chemical Industries Ltd. (Tokyo, Japan). Sodium dodecyl benzene sulfate (SDBS) and para-nitro benzenediazonium tetrafluoroborate were purchased from Tokyo Chemical Industry Co. Ltd. (Tokyo, Japan).

Preparation of surfactant-dispersed SWCNTs

To prepare the 2.0 wt% SDBS-dispersed SWCNTs solution, SWCNTs (5.0 mg) and a D_2O (20 mL) solution containing SDBS (2.0 wt%) were added to a 50 mL glass bottle. The mixture was sonicated in an ice bath using a bath-type sonicator (Branson 5510) for 1 h (180 W, 42 kHz) and a tip-type sonicator (UD-200, Tomy) for 30 min (200 W, 20 kHz). The dispersion was centrifuged at 147 000g (Hitachi Himac, CS 150 GX) for 4 h, and the supernatant (top 90%) was collected. A 2.0 wt% SDS-dispersed SWCNTs solution was prepared in a similar manner. D_2O was used to monitor the changes in the PL at approximately 1200 nm instead of H_2O to avoid the reabsorption of H_2O.

Synthesis of locally functionalized SWCNTs (lf-SWCNTs)

For lf-SWCNTs-pNO_2, a 0.2 wt% SDBS-dispersed SWCNTs solution in D_2O (39.6 mL) and a 1280 or 2560 μM para-nitro benzenediazonium tetrafluoroborate (Dz-pNO_2)[37] solution in D_2O (0.4 mL) were mixed and stirred at 30 °C for 24 h in the dark. SDBS was chosen because the reaction under SDS resulted in insufficient modification of the lf sites (data not shown).

For lf-SWCNTs-oP, a 0.2 wt% SDS-dispersed SWCNTs solution in D_2O (39.6 mL) and a 320 or 640 μM ortho-phenyl benzenediazonium tetrafluoroborate (Dz-oP)[52] solution in D_2O (0.4 mL) were mixed and stirred at 30 °C for 24 h in the dark. SDS was chosen because the use of SDBS-dispersed SWCNTs resulted in the generation the intense E_{11}^* PL peak together with E_{11}^{*-} PL.[52]

In our previous reports,[47,52,63–65] the reactions were carried out for one week in the dark without stirring. However, the reaction time was reduced by stirring, which was monitored by the change in the PL spectra (Fig. S1 and S2†).

Excess diazonium molecules were removed by dialysis for two days using a dialysis cassette (MWCO: 10 000) in a 0.2 wt% SDS in H_2O solution.[64] However, successive gel-coating without the removal of excess diazonium compounds resulted in poor

fractionation resolution in length sorting using column chromatography (data not shown).

Synthesis of *endo*-FpMMA

Methacrylate carrying the *endo*-form of the furan-protected maleimide (denoted as *endo*-FpMMA, see ^{1}H NMR spectra for Fig. S3†) was synthesized according to the reported procedure.[56,59] Briefly, first, the maleimide was protected with furan using a Diels–Alder reaction for five days in the dark at 25 °C and the *endo*-form furan-protected maleimide was coupled with PEGMA ($M_n \sim 500$) using the Mitsunobu reaction to afford *endo*-FpMMA.

CNT micelle polymerization

The concentration of SWCNTs was adjusted to an absorbance of 0.25 with an optical path length of 10 mm based on π plasmon absorption at 780 nm. This range was chosen because the absorbance is less affected by environmental and structural changes of SWCNTs compared to the inter-band transition peaks.[66] For the synthesis of gel-coated lf-SWCNTs-*p*NO$_2$, *endo*-FpMMA (60 mg, 10.5 mM), PEGMA (60 mg, 24 mM) and BIS (2.0 mg, 2.6 mM) were added to the 0.2 wt% SDS-dispersed SWCNTs solution (5.0 mL) in a 13.5 mL screw bottle and the resulting mixture was bubbled with N$_2$ gas to remove O$_2$ for 30 min. TMEDA (8.8 μL) and a 10 wt% aqueous solution of APS (25 μL) were added to the mixture. The polymerization reaction was then carried out at room temperature for 24 h under a N$_2$ atmosphere. The resulting solutions were filtered (MWCO: 200 000) ten times to remove SDS, unreacted monomers, and oligomers. The obtained gel-coated lf-SWCNTs-*p*NO$_2$ solutions were redispersed in D$_2$O after freeze-drying to spectra measurement. The gel-coated lf-SWCNTs-*o*P were synthesized using the same method.

Measurements

The UV-vis-NIR spectra were measured at 25 °C using a V-670 spectrophotometer (JASCO, Tokyo, Japan). PL spectra were measured using a NanoLOG-EXT spectrofluorometer (Horiba JOBIN YVON, Longjumeau, France). Typically, the measurements were performed using a quartz cell with a path length of 2 mm. The length fractionated SWCNTs solution was measured using a quartz cell with an optical path length of 10 mm.

Raman spectra were recorded at room temperature using a RAMANtouch spectrophotometer (Nanophoton, Osaka, Japan). The objective lens of the inverted microscope, excitation wavelength, grating, exposure time, and integration number were ×20, 532 nm, 600 g mm^{-1}, 2 s, and 5 times, respectively. Measurements were performed, focusing on SWCNTs dispersions in a 6 mL screw bottle. For the length-fractionated lf-SWCNTs, the solution was dropped onto a glass slide and dried, after which measurements were taken at five different points and the mean and standard deviation were calculated.

Atomic force microscopy (AFM) measurements (AC mode) were performed using an Agilent 5500 probe microscope (Agilent Technologies, California, U.S.A.) in air and the silicon cantilever PPP-NVSTR-W (NANOSENSORS, NanoWorld AG, Neuchatel, Switzerland). For the AFM sample preparation, the cleaved mica was soaked in a solution of 5 mL of 2-isopropanol and 50 μL of 3-aminopropyltriethoxysilane (APTES),[47,61] allowed to stand for 1 h, washed with Milli-Q water, and dried in air. 10 μL SWCNTs solutions were dropped onto the APTES-modified mica, allowed to stand at room temperature for 10 min, rinsed with 1 mL of Milli-Q water, and dried in air. AFM image processing was performed using Scanning Probe Image Processor (Ver. 6.2.6). The length of the lf-SWCNTs was determined based on the mean and standard deviation of the contour length of 100 randomly selected lf-SWCNTs in each sample. The height of the lf-SWCNTs was determined based on the mean and standard deviation of 50 randomly selected lf-SWCNTs by measuring the cross-sectional height at three points per one lf-SWCNTs.

Variable temperature PL measurements

The PL measurements of 1.0 wt% SDS- or SDBS-dispersed lf-SWCNTs in D$_2$O[67] and gel-coated lf-SWCNTs in D$_2$O at 25–65 °C [64] were performed with the following optical path length, excitation wavelength, exposure time, and repetition number at each temperature: 2 mm, 570 nm, 5 s, and three times, respectively. For length-fractionated gel-coated lf-SWCNTs in H$_2$O, the optical path length and exposure time were 10 mm and 60 s, respectively, and the errors calculated by the error propagation method from the estimated errors during peak deconvolution were displayed as error bars for each temperature. The dispersion stability of the lf-SWCNTs during the measurements was confirmed by verifying that the PL spectra remained unchanged before and after heat treatment. The obtained spectra were analyzed using the van't Hoff equation in accordance with several previous studies:[36,51,64,67]

$$\ln \frac{I_{11}}{I_{11}^*} = -\frac{\Delta E_{\text{thermal}}}{kT} + A$$

$$\Delta E_{\text{optical}} = \Delta E_{\text{thermal}} + \lambda$$

where I_{11} is the intensity of E_{11} PL, I_{11}^* is the intensity of E_{11}^* or E_{11}^{*-} PL, $\Delta E_{\text{thermal}}$ is the exciton detrapping energy [meV], k is the Boltzmann constant, T is the temperature [K], A is an arbitrary constant, $\Delta E_{\text{optical}}$ [meV] is the optical depth corresponding to an energy difference between E_{11} and E_{11}^* or E_{11}^{*-} PL, and λ is the reorganization energy [meV].

Length fractionation

Length fractionation of gel-coated lf-SWCNTs was performed using a previously reported method.[61] An HPLC system (SHIMADZU CORPORATION, Kyoto, Japan) was connected to COSMOSIL CNT-300, CNT-1000, and CNT-2000 SEC columns (Nacalai Tesque Inc.). The Tris-EDTA (TE) buffer was used as the mobile phase at a flow rate of 1.0 mL min^{-1}. To the gel-coated lf-SWCNTs solutions (1980 μL), ×100 TE buffer (20 μL) was added and filtered with a 0.45 μm filter. The concentration of the gel-coated lf-SWCNTs solution was adjusted to 5–6 nM (for the calculation of molar concentration of the gel-coated lf-SWCNTs, see "Estimation of the SWCNTs concentration" section). The

sample (200 μL) was injected, and the eluate was fractionated at 2.0 mL per fraction. The optical absorption of the eluate was monitored at 290 and 573 nm.

The estimated concentration of the gel-coated lf-SWCNTs in the fractions was approximately 0.05–0.7 nM, which was 50–100 times lower than that of the injected solutions (Table S1†), similar to our previous fractionation of unfunctionalized gel-coated SWCNTs,[61] indicating that the presence of aryl-modifications did not affect the fractionation.

Estimation of the SWCNTs concentration

The concentration of SWCNTs (C_{SWCNT}) was estimated using the following equation, based on previous studies:[44,68]

$$c_c = 5.1 \times 10^{-8} \times \frac{\Delta_{fwhm} \times OD_{S1}}{0.01 \times d}$$

$$c_{SWCNT} = \frac{c_c}{N_c} = \frac{c_c}{l_{SWCNT} \times N_{c/nm}}$$

where c_c [M] is the carbon concentration, Δ_{fwhm} is the full width at half maximum of the S_1 absorption spectrum of (6, 5)-SWCNTs, OD_{S1} is the S_1 absorbance of (6, 5)-SWCNTs, d [mm] is the optical path length, N_c is the number of carbon atoms in the SWCNTs, l_{SWCNT} is the average length of the SWCNTs, $N_{c/nm}$ is the number of carbon atoms per nm of SWCNTs (88 for (6, 5)-SWCNTs), and Δ_{fwhm} and OD_{S1} were determined by peak separation of absorption spectra measured using package Multi peak fitting in Igor Pro (ver. 6.36J).

Results and discussion

Two locally functionalized SWCNTs (lf-SWCNTs) were prepared by reacting a (6, 5)-rich SWCNTs with *para*-nitro benzenedia-zonium tetrafluoroborate (Dz-pNO$_2$)[37] and *ortho*-phenyl benze-nediazonium tetrafluoroborate (Dz-oP)[52] for 24 h in aqueous SDBS and SDS D$_2$O solutions, respectively (Fig. 1). To optimize the density of lf sites, the concentrations of the diazoniums (Dz-pNO$_2$ and Dz-oP) were varied. In the absorption spectra of lf-

SWCNTs modified with Dz-pNO$_2$ (lf-SWCNTs-pNO$_2$) and Dz-oP (lf-SWCNTs-oP), only a slight decrease in absorption at 980 nm was observed (Fig. S1a and S1d†). In contrast, new emission peaks assignable to E_{11}^* and E_{11}^{*-} PL were clearly observed at 1141 nm for lf-SWCNTs-pNO$_2$ (Fig. S1b†) and 1260 nm for lf-SWCNTs-oP (Fig. S1e†), respectively, indicating the successful introduction of the lf sites. The PL intensities increased as the concentration of Dz-pNO$_2$ and Dz-oP increased to 25.6 μM and 6.4 μM, respectively (Fig. S4†). Therefore, diazonium concentrations of 25.6 μM and 6.4 μM were used to prepare lf-SWCNTs-pNO$_2$ and lf-SWCNTs-oP, respectively.

0.2 wt% SDBS-dispersed lf-SWCNTs-pNO$_2$ and SDS-dispersed lf-SWCNTs-oP in D$_2$O were dialyzed with an SDS H$_2$O solution (0.2 wt%) for two days to remove residual diazo-nium reactants. For the lf-SWCNTs-pNO$_2$ solution, SDBS was replaced by SDS for the subsequent gel coating process that was conducted in the SDS solution. The disappearance of the absorption peak at 260 nm arising from SDBS indicated the successful replacement of SDBS with SDS (Fig. S5a†).[64] After dialysis, only a slight decrease in the absorption peaks was observed due to the decrease in concentration, confirming the good dispersion of the lf-SWCNTs (Fig. S5b–e†). In contrast, a large decrease in E_{11}^{*-} PL intensity at 1260 nm was observed for lf-SWCNTs-oP, probably because of the electron-to-solvent energy transfer (EVET)[69] from E_{11}^{*-} PL to H$_2$O absorption at 1200 nm (Fig. S5f†).

The two obtained lf-SWCNTs were coated with a gel *via* CNT micelle polymerization using a methacrylate monomer con-taining PEG (PEGMA; Fig. 1) to offer a stable dispersion in an aqueous system.[53,56,61] Methacrylate containing the furan group was also used as the co-monomer, which can be used for post-modification based on ene-thiol chemistry.[56,59,61] BIS and APS were used as the crosslinker and initiator, respectively (see Fig. S6† for the chemical structure of the gel). Previously, we reported that APS radicals introduced additional sp^3 defects depending on the APS concentration.[58,61,62] Therefore, in this study, the APS concentration was controlled to avoid the introduction of additional sp^3 lf sites. In the PL spectra ob-tained after polymerization, additional peaks were observed
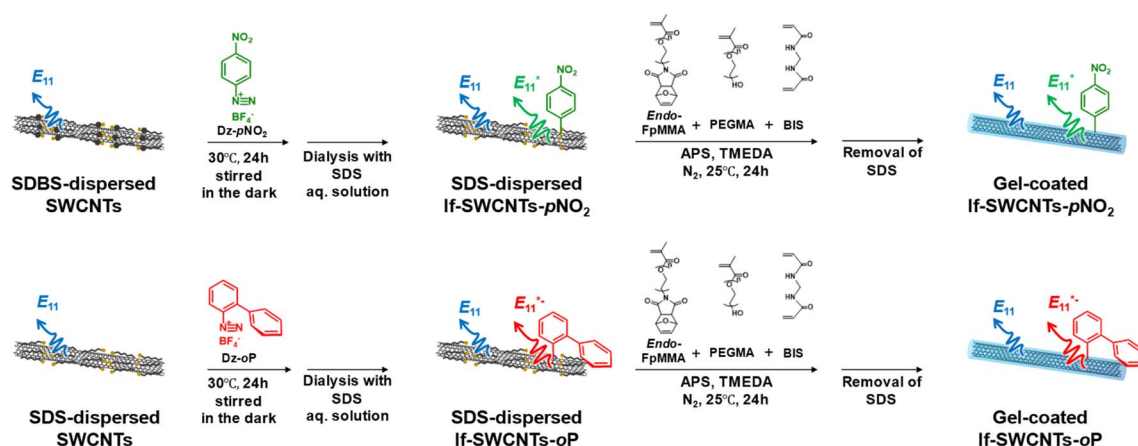

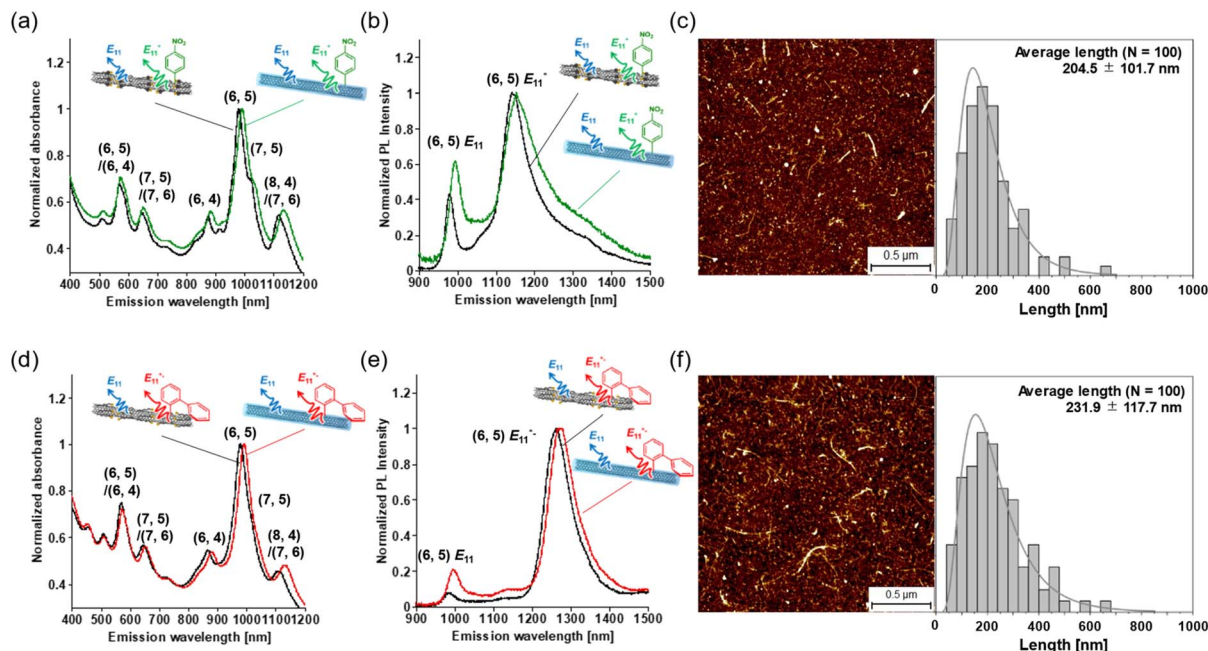**Fig. 1** Synthetic scheme of the gel-coated lf-SWCNTs-pNO$_2$ (upper) and gel-coated lf-SWCNTs-oP (lower).

Fig. 2 (a) Absorption and (b) PL spectra (excitation: 570 nm) of SDBS-dispersed lf-SWCNTs-pNO$_2$ (black) and gel-coated lf-SWCNTs-pNO$_2$ (green) in D$_2$O, (c) AFM image and length distribution of gel-coated lf-SWCNTs-pNO$_2$. (d) Absorption and (e) PL spectra (excitation: 570 nm) of SDS-dispersed lf-SWCNTs-oP (black) and gel-coated lf-SWCNTs-oP (red) in D$_2$O, and (f) AFM image and length distribution of gel-coated lf-SWCNTs-oP.

when the APS concentration exceeded 20 wt%, while no additional peak was observed when the concentration below 10 wt% (Fig. S7†). Therefore, 10 wt% APS was used for polymerization. The absence of additional sp^3 introduction was also confirmed by the identical D/G ratios in the Raman spectra after polymerization (Fig. S8†).

Fig. 2a shows the absorption spectra of lf-SWCNTs-pNO$_2$ and lf-SWCNTs-oP before and after gel coating. 12.0 nm (15 meV) and 12.6 nm (16 meV) red shifts were observed for lf-SWCNTs-pNO$_2$ and lf-SWCNTs-oP upon coating, respectively, in the E_{11} transition of (6, 5) of the absorption peak. For PL, 15.1 nm (19 meV) and 12.0 nm (11 meV) red shifts were observed for the (6, 5) E_{11} and E_{11}^* PL of lf-SWCNTs-pNO$_2$, respectively (Fig. 2b), whereas 13.0 nm (17 meV) and 11.9 nm (9 meV) red shifts were observed for the E_{11} and E_{11}^{*-} PL of lf-SWCNTs-oP, respectively (Fig. 2e). The results clearly show that the lf-SWCNTs were replaced from a hydrophobic surfactant environment to a hydrophilic gel environment. For both lf-SWCNTs, the PL from the lf sites (E_{11}^* and E_{11}^{*-}) exhibited smaller shifts than the PL from the pristine site (E_{11}). These differences are considered to reflect differences in the surface environment; namely, the water molecules were in good contact with the lf-SWCNTs surface in the gel environment, but such structures were disrupted at the lf sites, and the hydrophobic polymer chains were in contact, resulting in small changes from the hydrophobic surfactant environments. In particular, the smallest change was observed for the E_{11}^{*-} sites (9 meV) in lf-SWCNTs-oP, and the polymer-enriched environment might have affected the hydrophobicity of the pristine site, resulting in smaller shifts in E_{11} (17 meV) compared to the shifts in E_{11} for lf-SWCNTs-pNO$_2$ (19

meV). Similar hydrophobic environments in aryl-modified lf-SWCNTs were reported in our previous study using polymer-wrapping lf-SWCNTs.[64] The possible surface structure is illustrated in Fig. 3. It is also worth mentioning that the maintenance of clear PL indicates that the lf-SWCNTs were stably isolated by the gel coating (Fig. S9†).

We also noticed that the relative intensity of E_{11}^* PL in lf-SWCNTs-pNO$_2$ and E_{11}^{*-} PL in lf-SWCNTs-oP with respect to the E_{11} PL intensity decreased after gel coating, which is in good agreement with previous reports that non-radiative recombination of localized excitons in lf sites was more sensitive to the increase in dielectric shielding compared to those in pristine sites.[47,63,70]
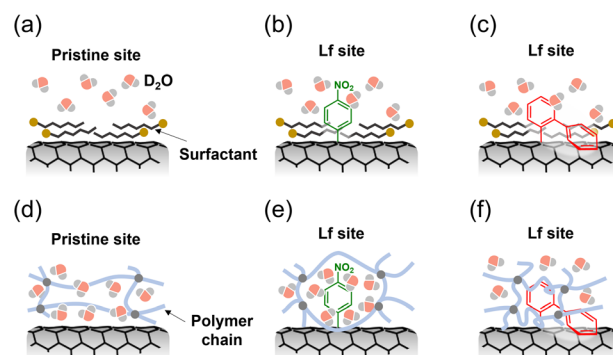

Fig. 3 Schematic diagram around the pristine site and lf site of (a and b) SDBS-dispersed lf-SWCNTs-pNO$_2$, (a and c) SDS-dispersed lf-SWCNTs-oP, (d and e) gel-coated lf-SWCNTs-pNO$_2$ and (d and f) gel-coated lf-SWCNTs-oP.

In the AFM images of the gel-coated lf-SWCNTs-pNO$_2$ (Fig. 2c) and lf-SWCNTs-oP (Fig. 2f), rod and spherical spots corresponding to gel-coated lf-SWCNTs and gel without lf-SWCNTs, respectively, were observed. From the statistical analysis of the lf-SWCNTs, the average length and height were 204.5 ± 101.7 nm and 1.77 ± 0.55 nm for lf-SWCNTs-pNO$_2$, respectively (Fig. 2c), and 231.9 ± 117.7 nm and 1.76 ± 0.63 nm for lf-SWCNTs-oP, respectively (Fig. 2f). The average height of the gel-coated lf-SWCNTs were comparable to that of gel-coated SWCNTs without locally functionalized modification.[61] Therefore, assuming that the average diameter of the CoMoCAT-SWCNT was 0.78 nm, the thickness of the gel was roughly 1 nm and the aryl substituents were buried in the gel layer (Fig. 3c and d).

Fig. 4a and b show temperature-dependent PL spectra of the gel-coated lf-SWCNTs-pNO$_2$ (Fig. 4a) and gel-coated lf-SWCNTs-oP (Fig. 4b) measured at different temperature (25–65 °C) in D$_2$O. The measurements were carried out wider range than the biological application temperature range (25–38 °C) to ensure the analytical accuracy as the previous reports also applied.[51,64,67,71] The PL intensity decreased with increasing temperature, especially for E_{11}^* PL (lf-SWCNTs-pNO$_2$) and E_{11}^{*-} PL (lf-SWCNTs-oP) rather than E_{11} PL, suggesting that the PL from the lf sites is useful as a temperature probe. The E_{11}^* and E_{11}^{*-} PL intensities of the gel-coated lf-SWCNTs changed significantly by approximately 50% and 30%, respectively, in the range of 25–65 °C, which is sufficiently large compared to other dye systems.[3] In contrast, the E_{11} PL of unfunctionalized gel-coated SWCNTs changed only slightly by approximately 20% (Fig. S10†). In Fig. 4c and d, the PL intensity ratios of E_{11} PL/E_{11}^* PL(I_{11}/I_{11}^*) and E_{11} PL/E_{11}^{*-} PL(I_{11}/I_{11}^{*-}) are plotted as a function of inverse temperature ($1/T$), and a clear linear relationship was obtained for $\ln(I_{11}/I_{11}^*)$ $vs.$ $1/T$ for lf-SWCNTs-pNO$_2$ (Fig. 4c) and $\ln(I_{11}/I_{11}^{*-})$ $vs.$ $1/T$ for lf-SWCNTs-oP (Fig. 4d). The same measurements were performed for the SDBS-dispersed lf-SWCNTs-pNO$_2$ and SDS-dispersed lf-SWCNTs-oP for comparison. The lower $\ln(I_{11}/I_{11}^*)$ and $\ln(I_{11}/I_{11}^{*-})$ values for the surfactant-dispersed lf-SWCNTs compared to the gel-coated lf-SWCNTs correspond to the brighter PL from the lf sites for the surfactant-dispersed lf-SWCNTs, as discussed above.

Assuming that the trapping/de-trapping of the excitons in the lf sites were thermodynamically reversible and PL spectra reflect the equilibrium state, these plots correspond to the van't Hoff plot, and therefore the energy change can be assignable to the de-trapping energies ($\Delta E_{\text{thermal}}$) of the E_{11}^* and E_{11}^{*-} excitons.[35,36,51,67,72] $\Delta E_{\text{thermal}}$ was smaller than the optical gap ($\Delta E_{\text{optical}}$) determined from the emission energies, and the difference was assigned as reorganization energies (λ).[51,67] From this relationship ($\Delta E_{\text{optical}} = \Delta E_{\text{thermal}} + \lambda$), λ values were calculated and summarized in Table 1. The λ of lf-SWCNTs involves several complex reorganization phenomena such as distortion of the SWCNTs crystal structure, exciton-phonon coupling, reorganization of surrounding molecules such as surfactants[67] and multiphonon decay (MPD).[36,69,72] However, in the current simplified model, identification of the origin of the reorganization energy was rather difficult similar to the previous study.[73]

Of interest, greater $\Delta E_{\text{thermal}}$ values were observed for lf-SWCNTs-pNO$_2$ systems compared to those of lf-SWCNTs-oP systems, although the $\Delta E_{\text{optical}}$ values were larger for lf-SWCNTs-oP than those of lf-SWCNTs-pNO$_2$, corresponding to the higher responsiveness of E_{11}^* PL than E_{11}^{*-} PL to temperature change. Zaumseil et $al.$ reported a similar trend for polymer-wrapped lf-SWCNTs in organic solvents ($\Delta E_{\text{thermal}}$ of $E_{11}^* = 79$ meV and $E_{11}^{*-} = 27$ meV)[36] and lf-SWCNTs on TiO$_x$ ($\Delta E_{\text{thermal}}$ of $E_{11}^* = 100$ meV and $E_{11}^{*-} = 36$ meV),[72] and they explained that MPD that is related to the interactions between localized excitons and phonons contributed to the larger λ in E_{11}^{*-}, yielding smaller $\Delta E_{\text{thermal}}$ values for E_{11}^{*-} PL. In contrast, when comparing gel-coated and surfactant-dispersed lf-
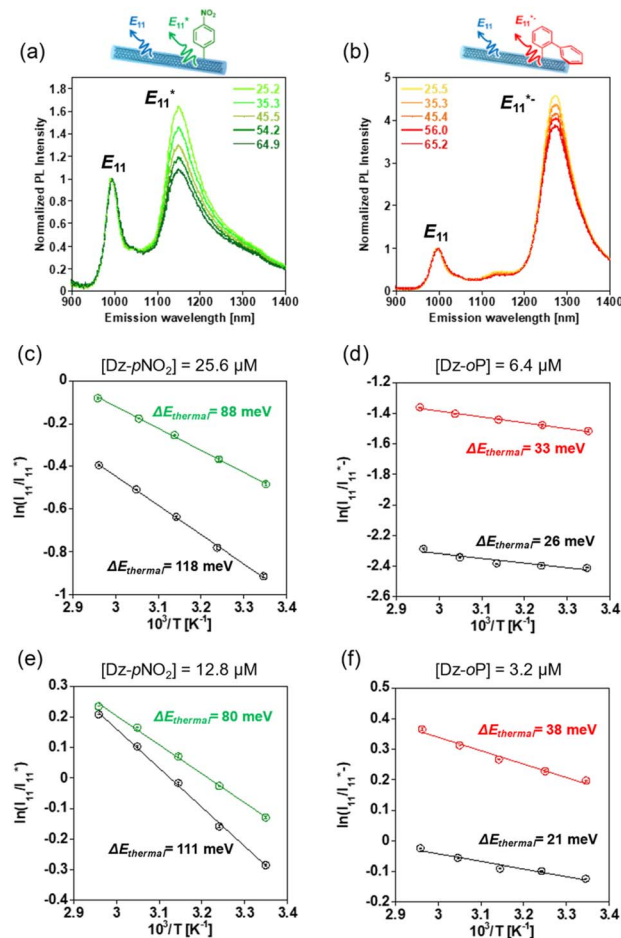

Fig. 4 PL spectra (excitation: 570 nm) of the (a) gel-coated lf-SWCNTs-pNO$_2$ solution and (b) gel-coated lf-SWCNTs-oP solution in D$_2$O upon increasing the temperature. The van't Hoff plot of the (c) gel-coated lf-SWCNTs-pNO$_2$ synthesized with [Dz-pNO$_2$] = 25.6 μM (green) and lf-SWCNTs-pNO$_2$ in SDBS synthesized with [Dz-pNO$_2$] = 25.6 μM (black), (d) gel-coated lf-SWCNTs-oP synthesized with [Dz-oP] = 6.4 μM (red) and SDS-dispersed lf-SWCNTs-oP synthesized with [Dz-oP] = 6.4 μM (black), (e) gel-coated lf-SWCNTs-pNO$_2$ synthesized with [Dz-pNO$_2$] = 12.8 μM (green) and SDBS-dispersed lf-SWCNTs-pNO$_2$ synthesized with [Dz-pNO$_2$] = 12.8 μM (black), and (f) gel-coated lf-SWCNTs-oP synthesized with [Dz-oP] = 3.2 μM (red) and SDS-dispersed lf-SWCNTs-oP synthesized with [Dz-oP] = 3.2 μM (black). Error bars mean standard deviation calculated from three times measurements.

Table 1 Calculated $\Delta E_{optical}$, $\Delta E_{thermal}$, and λ Values of lf-SWCNTs-pNO$_2$ in SDBS solution, gel-coated lf-SWCNT-pNO$_2$, lf-SWCNTs-oP in SDS solution, and gel-coated lf-SWCNTs-oP in D$_2$O

	Diazonium	$\Delta E_{optical}$ [meV]		$\Delta E_{thermal}$ [meV]		λ [meV]	
		Gel-coated	Surfactant	Gel-coated	Surfactant	Gel-coated	Surfactant
Lf-SWCNTs-pNO$_2$	25.6 μM	167	182	88	117	79	64
	12.8 μM	169	182	80	110	88	71
Lf-SWCNTs-oP	6.4 μM	269	276	33	26	236	250
	3.2 μM	269	278	38	21	231	257

SWCNTs, surfactant-dispersed lf-SWCNTs exhibited larger $\Delta E_{thermal}$ and smaller λ values for lf-SWCNTs-pNO$_2$ but a smaller $\Delta E_{thermal}$ and larger λ was obtained for lf-SWCNTs-oP. We consider that the water-rich environment of the gel layer (as discussed in Fig. 2) provides E_{11}^{*} excitons perturbated with solvent polarization, resulting in larger λ (smaller $\Delta E_{thermal}$) values for the gel-coated lf-SWCNTs-pNO$_2$.[64,73] In contrast, for E_{11}^{*-} PL, the environment with fewer water molecules induced by

the hydrophobic-oP reduced the dielectric constant and weakened the solvent polarization effect.[74–76] In addition, the rigid gel-enriched environment for the gel-coated lf-SWCNTs-oP further weakened the reorganization energy of the surrounding molecules compared to the dynamic surfactant environment, yielding smaller λ and higher responsiveness for the gel-coated lf-SWCNTs-oP. This highlights that a rigid gel environment with hydrophobic modification enables superior responsiveness of the lf sites.

Kim *et al.* reported that the distance between lf sites affected the temperature dependency of the PL (*e.g.* $\Delta E_{thermal}$ of excitons), and if the lf sites were close enough to interact with each other, the coupling localized exciton-phonon was reduced and the reduction of λ (=increase of $\Delta E_{thermal}$) occurred.[67] To verify this effect, lf-SWCNTs-pNO$_2$ and lf-SWCNTs-oP with lower defect densities were prepared using a lower diazonium concentration (lf-SWCNTs-pNO$_2$ ([Dz-pNO$_2$] = 12.8 μM) and lf-
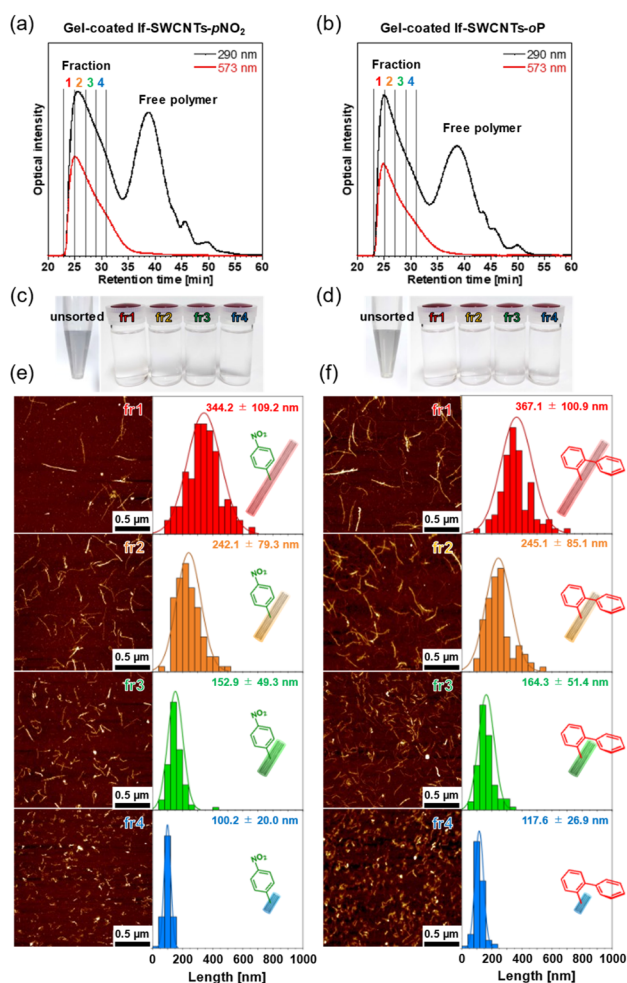

Fig. 5 (a and b) Size exclusion chromatograms, (c and d) photographs of fractionated solutions, and (e and f) AFM images and length distribution histogram of the (a–c) gel-coated lf-SWCNTs-pNO$_2$ and (d–f) gel-coated lf-SWCNTs-oP. Displayed values are the mean length ± standard deviation for $N = 100$.
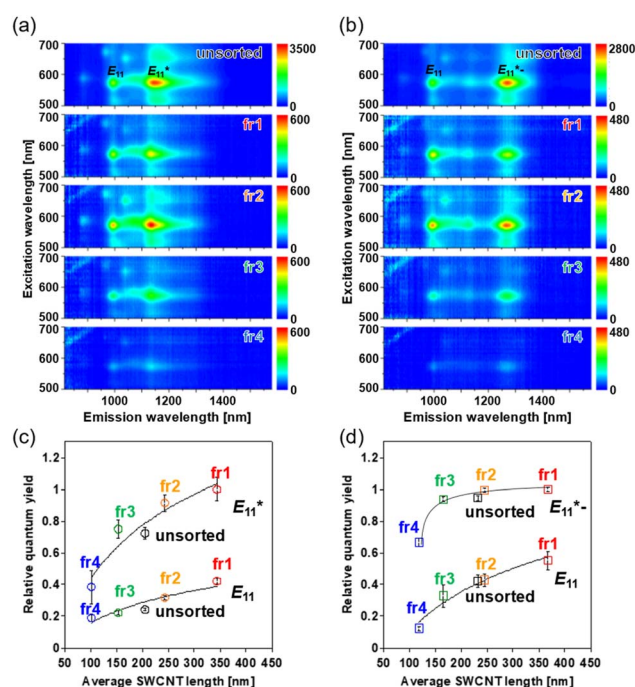

Fig. 6 (a and b) PL mapping and (c and d) relative quantum yield of length-sorted gel-coated lf-SWCNTs-pNO$_2$ and gel-coated lf-SWCNTs-oP, respectively, in H$_2$O. Curves are displayed as a guide to the eye. Error bars mean the error estimated during peak deconvolution.

SWCNTs-*o*P ([Dz-oP] = 3.2 μM)). We observed similar E_{11}, E_{11}^*, and E_{11}^{*-} PL red shifts from the surfactant environment to the gel coating, guaranteeing that similar dielectric environment changes were obtained for the lf sites (Fig. S11†). Fig. 4e and f show the van't Hoff plots of the gel-coated and surfactant-dispersed lf-SWCNTs-*p*NO₂ (Fig. 4e) and lf-SWCNTs-*o*P (Fig. 4f), respectively. For lf-SWCNTs-*p*NO₂, decreased $\Delta E_{thermal}$ (=lower responsiveness) values were observed as the defect density decreased, both for gel-coated (green line) and surfactant-dispersed (black line) lf-SWCNTs-*p*NO₂, as reported. In contrast, decreased $\Delta E_{thermal}$ (=increase of λ) values were observed only for surfactant-dispersed lf-SWCNTs-*o*P as the defect density decreased, but the opposite trend was observed for the gel-coated lf-SWCNTs-*o*P. The mechanism that explains this difference in behavior is unclear at this stage.

To study the effect of the edges of the tubes on the temperature response of the PL intensity, gel-coated lf-SWCNTs were fractionated by length using size exclusion chromatography.[61,77,78] We have reported that the gel coating offers stable dispersion upon chromatographic fractionation, and length separation is possible between approximately 100 to 400 nm. Fig. 5a and shows the chromatograms of the gel-coated lf-SWCNTs-*p*NO₂ (Fig. 5a) and lf-SWCNTs-*o*P (Fig. 5b) monitored at 290 nm (black line) and 573 nm (red line). At 573 nm, absorption of the E_{22} transition of lf-SWCNTs was observed, and at 290 nm, absorption of the lf-SWCNTs and gel was monitored.[61] Thus, the first peak (23–34 min) was assigned to the fraction containing lf-SWCNTs, while the second peak (35–50 min) was assigned to the gel without lf-SWCNTs. AFM analysis revealed that by fractionating the first peak, lf-SWCNTs-*p*NO₂ were obtained with lengths of 344.2 ± 109.2 (fr1), 242.1 ± 79.3 (fr2), 152.9 ± 49.3 (fr3), and 100.2 ± 20.0 nm (fr4) (Fig. 5e). For the gel-coated lf-SWCNTs-*o*P, the lf-SWCNTs were obtained with lengths of 367.1 ± 100.9 (fr1), 245.1 ± 85.1 (fr2), 164.3 ± 51.4
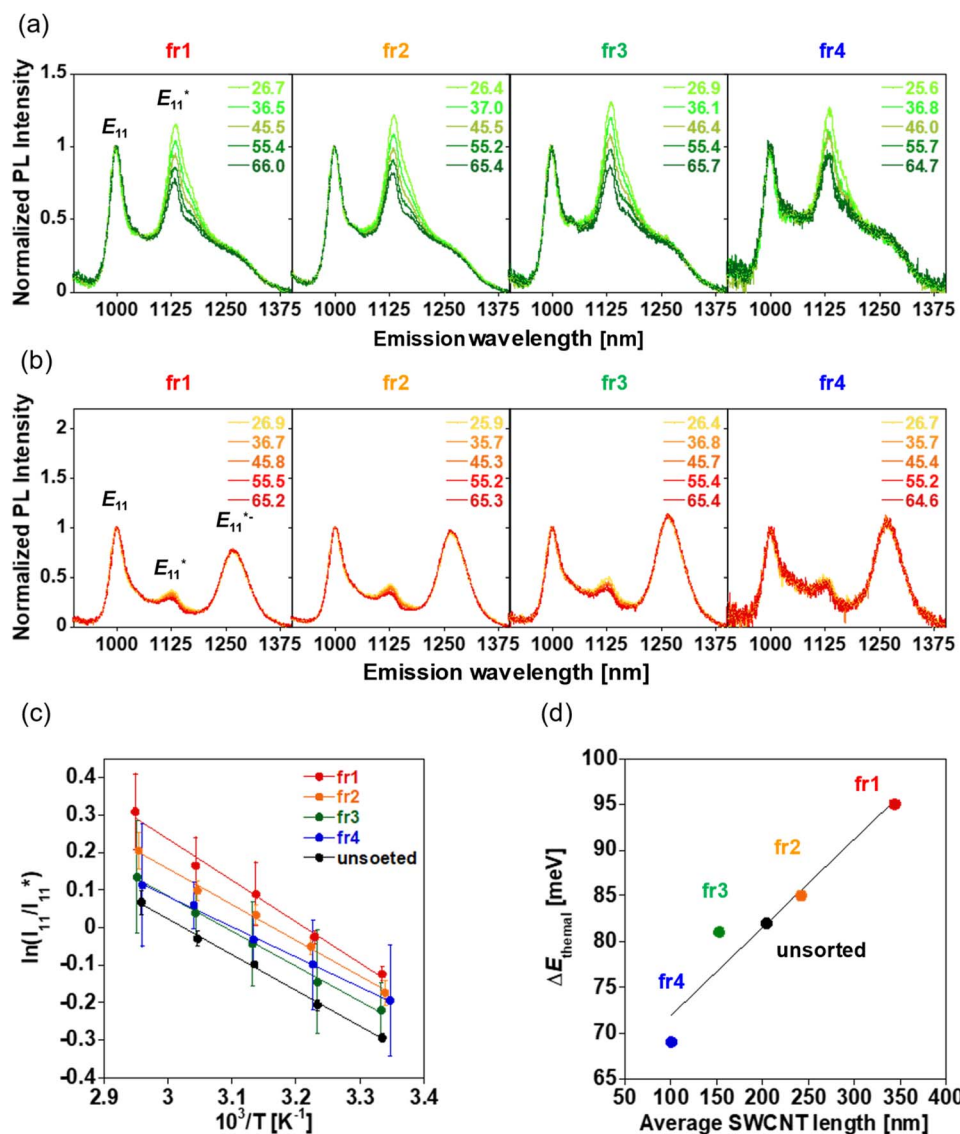

Fig. 7 Temperature-dependent PL spectra (excitation: 570 nm) of the length-sorted (a) gel-coated lf-SWCNTs-*p*NO₂ solution and (b) gel-coated lf-SWCNTs-*o*P solution in H₂O, (c) the van't Hoff plot of the length-sorted and unsorted gel-coated lf-SWCNTs-*p*NO₂ solution, and (d) plot of $\Delta E_{thermal}$ as a function of the average SWCNT length. Error bars mean the error estimated during peak deconvolution.

(fr3), and 117.6 ± 26.9 nm (fr4) (Fig. 5f). The length was within the standard deviation range for each fraction and was consistent with the gel-coated SWCNTs without lf sites reported previously,[61] indicating that the introduction of aryl-substituted groups did not affect the length fractionation. In the Raman spectra, shorter lf-SWCNTs exhibited higher D/G ratios, clearly indicating that the tube ends had a stronger effect on shorter lf-SWCNTs (Fig. S12†).[34,79]

Fig. 6a and b show the PL contour plots of the gel-coated lf-SWCNTs-pNO$_2$ (Fig. 6a) and lf-SWCNTs-oP (Fig. 6b) in TE buffer. lf-PL spots were clearly observed in all fractions due to aryl defects. The differences in the PL intensity were due to the different concentrations of lf-SWCNTs in each fraction (Fig. S13 and Table S1†). The relative quantum yields of the (6, 5)-SWCNTs were calculated based on the ratio of the integral of the E_{11}, E_{11}^*, and E_{11}^{*-} PL peak areas at 570 nm excitation to the integral of the E_{22} absorption peak area (Fig. 6c and d). For E_{11} PL, higher relative quantum yields were achieved for longer lf-SWCNTs, as observed for the gel-coated SWCNTs without lf sites,[61] indicating that the presence of lf sites did not affect the quenching behavior at the tube ends. The relative quantum yields of E_{11}^* and E_{11}^{*-} PL exhibited the same trend, but the increase in the yield was smaller for E_{11}^{*-} PL (>150 nm). These results can be explained by the difference in the optical trapping depths of the localized excitons in E_{11}^* (~170 meV) and E_{11}^{*-} (~270 meV); namely, the deeper trapping for E_{11}^{*-} is less sensitive for tube ends due to the lower concentration of excitons diffused to the tube ends.

Fig. 7a and b show the temperature-dependent PL (570 nm excitation) for the gel-coated lf-SWCNTs-pNO$_2$ (Fig. 7a) and lf-SWCNTs-oP (Fig. 7b) with different lengths. The solutions were desalted before the measurements to eliminate the effects of pH changes with temperature. For the gel-coated lf-SWCNTs-pNO$_2$, the PL intensity of E_{11}^* decreased with increasing temperature, whereas E_{11}^{*-} PL of lf-SWCNTs-oP showed negligible changes with temperature. Such insensitivity observed for lf-SWCNTs-oP was different from the unsorted lf-SWCNTs-oP discussed in Fig. 4. This clear difference can be explained by the difference of the solvent used. For length-fractionated lf-SWCNTs, the PL measurements were performed with H$_2$O used as the mobile phase for the chromatography and the absorption of H$_2$O at around 1200 nm caused EVET for E_{11}^{*-} PL.[69] In fact, the similar insensitivity was observed for the unsorted lf-SWCNTs-oP measured in H$_2$O (Fig. S14†).

Fig. 7c shows the van't Hoff plots of the gel-coated lf-SWCNTs-pNO$_2$ (see Fig. S15 and Table S2† for the gel-coated lf-SWCNTs-oP). Interestingly, as the length increased, E_{11}^* PL became more temperature sensitive and an increase in $\Delta E_{\text{thermal}}$ was observed (Fig. 7d and Table 2), while λ decreased. The relative temperature sensitivity ($S_{\text{rel}} = |\Delta E_{\text{thermal}}/kT^2| \times 100\%$)[15] at 310.15 K (37 °C) in H$_2$O were calculated and S_{rel} of unsorted, fr1, fr2, fr3 and fr4 of gel-coated lf-SWCNTs-pNO$_2$ were determined to be 0.99, 1.15, 1.03, 0.98 and 0.83% K^{-1}, respectively, which is quite high compared to the other reports.[3] However, this difference did not originate from the difference in E_{11}^* PL, but the difference in E_{11} PL, namely E_{11} PL quenching, predominantly occurred for shorter lf-SWCNTs (Fig. 6c) that

Table 2 Calculated $\Delta E_{\text{optical}}$, $\Delta E_{\text{thermal}}$, and λ values of the unsorted and length-sorted gel-coated lf-SWCNTs-pNO$_2$ in H$_2$O

Sample	Average SWCNT length [nm]	$\Delta E_{\text{optical}}$ [meV]	$\Delta E_{\text{thermal}}$ [meV]	λ [meV]
Unsorted	204.5	150	82	68
Fr1	344.2	153	95	58
Fr2	242.1	151	85	66
Fr3	152.9	152	81	72
Fr4	100.2	151	69	82

affected (I_{11}/I_{11}^*). This result suggests that length is an important factor, especially for short SWCNTs, when discussing the thermodynamic behavior of each site.[67] Regardless, as long as I_{11}/I_{11}^* is used as the temperature indicator, the longer lf-SWCNTs-pNO$_2$ is a better option. If the tube ends can function as lf sites,[71] the temperature responsiveness will be maintained for short SWCNTs.

Conclusions

The temperature dependence of PL in the NIR-II region from the sp^3 quantum defect sites (lf sites) was studied using surfactant-dispersed and gel-coated lf-SWCNTs with different PL (E_{11}^* and E_{11}^{*-}). As the temperature increased, the PL intensity from both the lf and non-lf sites decreased; however, the PL changes at the lf sites were more sensitive to temperature changes. Thus, ratiometric analysis of E_{11}/E_{11}^* and E_{11}/E_{11}^{*-} were conducted, and we found that E_{11}^* PL showed higher responsiveness (greater $\Delta E_{\text{thermal}}$) than E_{11}^{*-} PL because of the smaller reorganization energies (λ) of the E_{11}^* sites, especially for the surfactant-dispersed lf-SWCNTs. This study also revealed that the hydrophobicity of both the surrounding molecules and the modified aryl group played an important role. Hydrophilic groups, such as -pNO$_2$, induce a water-rich structure in the gel environment, which had a negative impact on temperature responsiveness compared to a hydrophobic surfactant environment. In contrast, hydrophobic groups, such as -oP, induce water-poor structures and rigid gel environments, which had a positive impact on responsiveness compared with dynamic surfactant environments. In terms of defect density, greater temperature responsiveness was observed in E_{11}^* PL lf-SWCNTs with a higher defect density due to the weakening of λ by the interaction between lf sites through localized exciton–phonon coupling. Regarding the length dependence, longer lf-SWCNTs exhibited higher temperature responsiveness due to tube-end quenching of E_{11} excitons than short lf-SWCNTs. As both the hydrophobicity of the aryl group and the gel structure can be tuned by molecular design, we believe that biocompatible gel-coated lf-SWCNTs-based temperature sensors with high responsiveness can be designed using NIR-II PL. One of the advantages to use lf-SWCNTs is the use of ratiometric analysis using both E_{11} and E_{11}^* PL (or E_{11}^{*-} PL) that allows us to distinguish the change of SWCNTs concentration.

Many studies to date have clarified the non-radiative pathways of localized exciton in lf-SWCNTs. However, due to the very

simplified models of reorganization energy and van't Hoff equation, this study has not yet determined the detailed reorganization energy λ. In the future, a detailed population dynamics model of mobile/localized excitons that considers the finite length effect of lf-SWCNTs, solvent polarity, and defect substituent polarity will need to be proposed to clarify the details of the reorganization energy of localized excitons. In addition, research is underway in our laboratory to demonstrate the usefulness of PL ratiometric local temperature sensors in cells and biological tissues.

Data availability

The data supporting this article have been included as part of the ESI.†

Author contributions

Ryo Hamano: conceptualization, data curation, investigation, methodology, formal analysis, writing – original draft, funding acquisition. Yoshiaki Niidome: result discussion. Naoki Tanaka: result discussion. Tomohiro Shiraki: result discussion. Tsuyohiko Fujigaya: conceptualization, project administration, result discussion, supervision, writing – review & editing, funding acquisition. The manuscript was written through the contributions of all authors. All authors have given approval to the final version of the manuscript.

Conflicts of interest

There are no conflicts to declare.

Acknowledgements

References

1 T. Bai and N. Gu, *Small*, 2016, **12**, 4590–4610.

2 C. D. S. Brites, P. P. Lima, N. J. O. Silva, A. Millán, V. S. Amaral, F. Palacio and L. D. Carlos, *Nanoscale*, 2012, **4**, 4799–4829.

3 A. Bednarkiewicz, L. Marciniak, L. D. Carlos and D. Jaque, *Nanoscale*, 2020, **12**, 14405–14421.

4 X.-d. Wang, X.-h. Song, C.-y. He, C. J. Yang, G. Chen and X. Chen, *Anal. Chem.*, 2011, **83**, 2434–2437.

5 F. Ye, C. Wu, Y. Jin, Y.-H. Chan, X. Zhang and D. T. Chiu, *J. Am. Chem. Soc.*, 2011, **133**, 8146–8149.

6 J.-M. Yang, H. Yang and L. Lin, *ACS Nano*, 2011, **5**, 5067–5071.

7 L. M. Maestro, C. Jacinto, U. R. Silva, F. Vetrone, J. A. Capobianco, D. Jaque and J. G. Sole, *Small*, 2011, **7**, 1774–1778.

8 Y. Zhao, X. Wang, Y. Zhang, Y. Li and X. Yao, *J. Alloys Compd.*, 2020, **817**, 152691.

9 D. Manzani, J. F. d. S. Petruci, K. Nigoghossian, A. A. Cardoso and S. J. L. Ribeiro, *Sci. Rep.*, 2017, **7**, 41596.

10 S. Chuma, K. Kiyosue, T. Akiyama, M. Kinoshita, Y. Shimazaki, S. Uchiyama, S. Sotoma, K. Okabe and Y. Harada, *Nat. Commun.*, 2024, **15**, 3473.

11 G. Kucsko, P. C. Maurer, N. Y. Yao, M. Kubo, H. J. Noh, P. K. Lo, H. Park and M. D. Lukin, *Nature*, 2013, **500**, 54–58.

12 I. Mokni, S. Slimi, A. Badri, R. Maria Solé, M. Aguiló, F. Díaz, B. Ayed and X. Mateos, *Ceram. Int.*, 2024, **50**, 22936–22946.

13 L. Marciniak, W. M. Piotrowski, M. Drozd, V. Kinzhybalo, A. Bednarkiewicz and M. Dramicanin, *Adv. Opt. Mater.*, 2022, **10**, 2102856.

14 A. Zhang, Z. Sun, M. Jia, G. Liu, F. Lin and Z. Fu, *Chem. Eng. J.*, 2019, **365**, 400–404.

15 A. Nexha, J. J. Carvajal, M. C. Pujol, F. Díaz and M. Aguiló, *J. Mater. Chem. C*, 2020, **8**, 180–191.

16 V. Gonzalez, D. A. L. Vignati, C. Leyval and L. Giamberini, *Environ. Int.*, 2014, **71**, 148–157.

17 K. T. Rim, K. H. Koo and J. S. Park, *Saf. Health Work*, 2013, **4**, 12–26.

18 S. Iijima and T. Ichihashi, *Nature*, 1993, **363**, 603–605.

19 S. M. B. Michael, J. O'Connell, C. B. Huffman, V. C. Moore, M. S. Strano, E. H. Haroz, K. L. Rialon, P. J. Boul, W. H. Noon, K. Carter, J. Ma, R. H. Hauge, R. Bruce Weisman and R. E. Smalley, *Science*, 2002, **297**, 593–596.

20 Y. Yomogida, T. Tanaka, M. Zhang, M. Yudasaka, X. Wei and H. Kataura, *Nat. Commun.*, 2016, **7**, 12056.

21 J. T. Robinson, G. Hong, Y. Liang, B. Zhang, O. K. Yaghi and H. Dai, *J. Am. Chem. Soc.*, 2012, **134**, 10664–10669.

22 J. Lefebvre, P. Finnie and Y. Homma, *Phys. Rev. B:Condens. Matter Mater. Phys.*, 2004, **70**, 045419.

23 K. Yoshino, T. Kato, Y. Saito, J. Shitaba, T. Hanashima, K. Nagano, S. Chiashi and Y. Homma, *ACS Omega*, 2018, **3**, 4352–4356.

24 J. H. Choi and M. S. Strano, *Appl. Phys. Lett.*, 2007, **90**, 223114.

25 T. T. S. Lew, V. B. Koman, K. S. Silmore, J. S. Seo, P. Gordiichuk, S. Y. Kwak, M. Park, M. C. Ang, D. T. Khong, M. A. Lee, M. B. Chan-Park, N. H. Chua and M. S. Strano, *Nat. Plants*, 2020, **6**, 404–415.

26 T. T. S. Lew, M. Park, J. Cui and M. S. Strano, *Adv. Mater.*, 2021, **33**, 2005683.

27 S. Kruss, D. P. Salem, L. Vuković, B. Lima, E. Vander Ende, E. S. Boyden and M. S. Strano, *Proc. Natl. Acad. Sci. U. S. A.*, 2017, **114**, 1789–1794.

28 M. H. Wong, J. P. Giraldo, S. Y. Kwak, V. B. Koman, R. Sinclair, T. T. Lew, G. Bisker, P. Liu and M. S. Strano, *Nat. Mater.*, 2017, **16**, 264–272.

29 J. J. Crochet, J. G. Duque, J. H. Werner, B. Lounis, L. Cognet and S. K. Doorn, *Nano Lett.*, 2012, **12**, 5091–5096.

30 A. Rajan, M. S. Strano, D. A. Heller, T. Hertel and K. Schulten, *J. Phys. Chem. B*, 2008, **112**, 6211–6213.

31 T. Hertel, S. Himmelein, T. Ackermann, D. Stich and J. Crochet, *ACS Nano*, 2010, **4**, 7161–7168.

32 T. K. Cherukuri, D. A. Tsyboulski and R. B. Weisman, *ACS Nano*, 2012, **6**, 843–850.

33 A. V. Naumov, D. A. Tsyboulski, S. M. Bachilo and R. B. Weisman, *Chem. Phys.*, 2013, **422**, 255–263.

34 J. A. Fagan, J. R. Simpson, B. J. Bauer, S. H. De Paoli Lacerda, M. L. Becker, J. Chun, K. B. Migler, A. R. Hight Walker and E. K. Hobbie, *J. Am. Chem. Soc.*, 2007, **129**, 10607–10612.

35 S. Ghosh, S. M. Bachilo, R. A. Simonette, K. M. Beckingham and R. B. Weisman, *Science*, 2010, **330**, 1656–1659.

36 S. Settle, F. J. Berger, S. Lindenthal, S. Zhao, A. A. El Yumin, N. F. Zorn, A. Asyuda, M. Zharnikov, A. Högele and J. Zaumseil, *Nat. Commun.*, 2021, **12**, 2119.

37 Y. Piao, B. Meany, L. R. Powell, N. Valley, H. Kwon, G. C. Schatz and Y. Wang, *Nat. Chem.*, 2013, **5**, 840–845.

38 T. Shiraki, Y. Miyauchi, K. Matsuda and N. Nakashima, *Acc. Chem. Res.*, 2020, **53**, 1846–1859.

39 J. Zaumseil, *Adv. Opt. Mater.*, 2021, **10**, 2101576.

40 Y. Maeda, P. Zhao and M. Ehara, *Chem. Commun.*, 2023, **59**, 14497–14508.

41 M. Kim, C. Chen, Z. Yaari, R. Frederiksen, E. Randall, J. Wollowitz, C. Cupo, X. Wu, J. Shah, D. Worroll, R. E. Lagenbacher, D. Goerzen, Y.-M. Li, H. An, Y. Wang and D. A. Heller, *Nat. Chem. Biol.*, 2023, **19**, 1448–1457.

42 S. Settle, C. A. Schrage, S. Jung, E. Michel, H. Li, B. S. Flavel, A. S. K. Hashmi, S. Kruss and J. Zaumseil, *Nat. Commun.*, 2024, **15**, 706.

43 M. Kim, J. J. McCann, J. Fortner, E. Randall, C. Chen, Y. Chen, Z. Yaari, Y. Wang, R. L. Koder and D. A. Heller, *J. Am. Chem. Soc.*, 2024, **146**, 12454–12462.

44 F. A. Mann, P. Galonska, N. Herrmann and S. Kruss, *Nat. Protoc.*, 2022, **17**, 727–747.

45 J. T. Metternich, J. A. C. Wartmann, L. Sistemich, R. Nißler, S. Herbertz and S. Kruss, *J. Am. Chem. Soc.*, 2023, **145**, 14776–14783.

46 C. Ma, J. M. Mohr, G. Lauer, J. T. Metternich, K. Neutsch, T. Ziebarth, A. Reiner and S. Kruss, *Nano Lett.*, 2024, **24**, 2400–2407.

47 Y. Niidome, R. Hamano, K. Nakamura, S. Qi, S. Ito, B. Yu, Y. Nagai, N. Tanaka, T. Mori, Y. Katayama, T. Fujigaya and T. Shiraki, *Carbon*, 2024, **216**, 118533.

48 Y. Iizumi, M. Yudasaka, J. Kim, H. Sakakita, T. Takeuchi and T. Okazaki, *Sci. Rep.*, 2018, **8**, 6272.

49 T. Takeuchi, Y. Iizumi, M. Yudasaka, S. Kizaka-Kondoh and T. Okazaki, *Bioconjug. Chem.*, 2019, **30**, 1323–1330.

50 Y. Niidome, R. Wakabayashi, M. Goto, T. Fujigaya and T. Shiraki, *Nanoscale*, 2022, **14**, 13090–13097.

51 H. Kwon, M. Kim, B. Meany, Y. Piao, L. R. Powell and Y. Wang, *J. Phys. Chem. C*, 2015, **119**, 3733–3739.

52 B. Yu, S. Naka, H. Aoki, K. Kato, D. Yamashita, S. Fujii, Y. K. Kato, T. Fujigaya and T. Shiraki, *ACS Nano*, 2022, **16**, 21452–21461.

53 Y. Tsutsumi, T. Fujigaya and N. Nakashima, *RSC Adv.*, 2014, **4**, 6318–6323.

54 Y. Tsutsumi, T. Fujigaya and N. Nakashima, *Nanoscale*, 2015, **7**, 19534–19539.

55 Y. Tsutsumi, T. Fujigaya and N. Nakashima, *Chem. Lett.*, 2016, **45**, 274–276.

56 Y. Nagai, Y. Tsutsumi, N. Nakashima and T. Fujigaya, *J. Am. Chem. Soc.*, 2018, **140**, 8544–8550.

57 Y. Nagai, M. Yudasaka, H. Kataura and T. Fujigaya, *Chem. Commun.*, 2019, **55**, 6854–6857.

58 Y. Nagai, K. Nakamura, M. Yudasaka, T. Shiraki and T. Fujigaya, *ACS Appl. Nano Mater.*, 2020, **3**, 8840–8847.

59 Y. Nagai, K. Nakamura, J. Ohno, M. Kawaguchi and T. Fujigaya, *ACS Appl. Bio Mater.*, 2021, **4**, 5049–5056.

60 S. S. Y. Law, G. Liou, Y. Nagai, J. Gimenez-Dejoz, A. Tateishi, K. Tsuchiya, Y. Kodama, T. Fujigaya and K. Numata, *Nat. Commun.*, 2022, **13**, 2417.

61 R. Hamano, N. Tanaka and T. Fujigaya, *Mater. Adv.*, 2024, **5**, 2482–2490.

62 Y. Nagai, R. Hamano, K. Nakamura, I. A. Widjaja, N. Tanaka, M. Zhang, T. Tanaka, H. Kataura, M. Yudasaka and T. Fujigaya, *Carbon*, 2024, **218**, 118728.

63 T. Shiraki, Y. Niidome, F. Toshimitsu, T. Shiraishi, T. Shiga, B. Yu and T. Fujigaya, *Chem. Commun.*, 2019, **55**, 3662–3665.

64 Y. Niidome, H. Matsumoto, R. Hamano, K. Kato, T. Fujigaya and T. Shiraki, *J. Phys. Chem. C*, 2024, **128**, 5146–5155.

65 B. Yu, T. Fujigaya and T. Shiraki, *Bull. Chem. Soc. Jpn.*, 2023, **96**, 127–132.

66 J. A. Fagan, M. L. Becker, J. Chun, P. Nie, B. J. Bauer, J. R. Simpson, A. Hight-Walker and E. K. Hobbie, *Langmuir*, 2008, **24**, 13880–13889.

67 M. Kim, L. Adamska, N. F. Hartmann, H. Kwon, J. Liu, K. A. Velizhanin, Y. Piao, L. R. Powell, B. Meany, S. K. Doorn, S. Tretiak and Y. Wang, *J. Phys. Chem. C*, 2016, **120**, 11268–11276.

68 F. Schöppler, C. Mann, T. C. Hain, F. M. Neubauer, G. Privitera, F. Bonaccorso, D. Chu, A. C. Ferrari and T. Hertel, *J. Phys. Chem. C*, 2011, **115**, 14682–14686.

69 X. He, K. A. Velizhanin, G. Bullard, Y. Bai, J.-H. Olivier, N. F. Hartmann, B. J. Gifford, S. Kilina, S. Tretiak, H. Htoon, M. J. Therien and S. K. Doorn, *ACS Nano*, 2018, **12**, 8060–8070.

70 Y. Niidome, B. Yu, G. Juhasz, T. Fujigaya and T. Shiraki, *J. Phys. Chem. C*, 2021, **125**, 12758–12766.

71 N. Danné, M. Kim, A. G. Godin, H. Kwon, Z. Gao, X. Wu, N. F. Hartmann, S. K. Doorn, B. Lounis, Y. Wang and L. Cognet, *ACS Nano*, 2018, **12**, 6059–6065.

72 S. Wieland, A. A. El Yumin, S. Settle and J. Zaumseil, *J. Phys. Chem. C*, 2024, **128**, 2012–2021.

73 V. Vaissier, P. Barnes, J. Kirkpatrick and J. Nelson, *Phys. Chem. Chem. Phys.*, 2013, **15**, 4804–4814.

74 Y. Ohno, S. Iwasaki, Y. Murakami, S. Kishimoto, S. Maruyama and T. Mizutani, *Phys. Status Solidi B*, 2007, **244**, 4002–4005.

75 R. Haggenmueller, S. S. Rahatekar, J. A. Fagan, J. Chun, M. L. Becker, R. R. Naik, T. Krauss, L. Carlson, J. F. Kadla, P. C. Trulove, D. F. Fox, H. C. DeLong, Z. Fang, S. O. Kelley and J. W. Gilman, *Langmuir*, 2008, **24**, 5070–5078.

76 G. Bisker, J. Dong, H. D. Park, N. M. Iverson, J. Ahn, J. T. Nelson, M. P. Landry, S. Kruss and M. S. Strano, *Nat. Commun.*, 2016, **7**, 10241.

77 X. Huang, R. S. McLean and M. Zheng, *Anal. Chem.*, 2005, **77**, 6225–6228.

78 C. Y. Khripin, X. Tu, J. M. Heddleston, C. Silvera-Batista, A. R. Hight Walker, J. Fagan and M. Zheng, *Anal. Chem.*, 2013, **85**, 1382–1388.

79 S. G. Chou, H. Son, J. Kong, A. Jorio, R. Saito, M. Zheng, G. Dresselhaus and M. S. Dresselhaus, *Appl. Phys. Lett.*, 2007, **90**, 131109.